Journal of Colloid and Interface Science 626 (2022) 591–598

Contents lists available at ScienceDirect

Journal of Colloid and Interface Science

journal homepage: www.elsevier.com/locate/jcis

Unraveling the role of hydrogen bromide in the growth of cesium lead bromide perovskite nanocrystals

Jingjing Cao, Qungui Wang, Wen Li, Cheng Yan, Xiankan Zeng, Yue Gao, Xiaotong Zheng, Jun Lu *, Weiqing Yang *

Key Laboratory of Advanced Technologies of Materials (Ministry of Education),School of Materials Science and Engineering, State Key Laboratory of Traction Power, Southwest Jiaotong University, Chengdu 610031, PR China

GRAPHICAL ABSTRACT

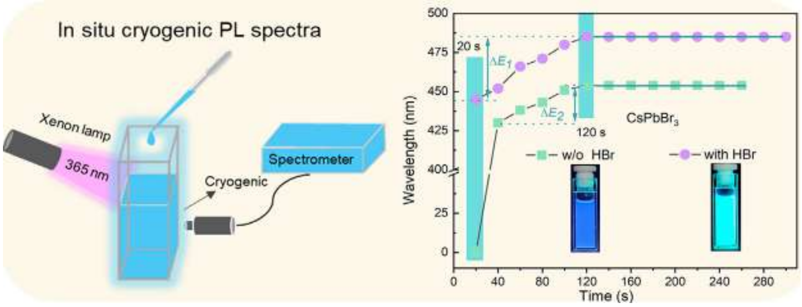

ARTICLE INFO

Article history:
Received 8 February 2022
Revised 26 May 2022
Accepted 28 June 2022
Available online 3 July 2022

Keywords:
Hydrogen bromide
Cesium lead bromide perovskite nanocrystals
Growth dynamics
in situ cryogenic PL spectra
Perovskite light-emitting diodes

ABSTRACT

Hydrogen bromide (HBr) could substantially improve the quality of cesium lead bromide perovskite ($CsPbBr_3$) nanocrystals (NCs) and greatly enhance their optoelectronic performance. However, clarifying the role of HBr in the growth of $CsPbBr_3$ NCs has been a substantial challenge thus far. Herein, we design an in situ cryogenic photoluminescence system using liquid nitrogen to unravel the role played by HBr in the growth of $CsPbBr_3$ NCs. Compared with no HBr (~40 s), HBr improves the nucleation rate of $CsPbBr_3$ NCs about two times (~20 s), and its emission peak also exhibits a redshift of ~30 nm. Thus, we conclude that HBr accelerates the nucleation rate of $CsPbBr_3$ NCs and extends their growth stage, affording the generation of large grains. Perovskite light-emitting diodes based on $CsPbBr_3$ NCs with added HBr also exhibit an outstanding performance. These outcomes provide new insights into the role of HBr in $CsPbBr_3$ NCs and help prepare high-quality $CsPbBr_3$ NCs for use in the fabrication of efficient $CsPbBr_3$ NC-based optoelectronic devices.

1. Introduction

All inorganic cesium lead bromide ($CsPbX_3$, X = Cl, Br and I) perovskite nanocrystals (NCs) have attracted considerable attention owing to their outstanding performances in optoelectronic and photovoltaic device applications [1,2], such as light-emitting diodes (LEDs) [3–6], solar cells [7,8], lasers, and photodetectors [8,9]. In particular, $CsPbX_3$ NCs, prepared using a simple solution-based synthesis method, possess excellent characteristics, such as a high photoluminescence quantum yield (PLQY), a narrow full width of half maximum (FWHM), a high color purity, broad wavelength tunability, and a high defect tolerance [10,11]. However, the

---

* Corresponding authors.
E-mail addresses: Junlyuprc@hotmail.com (J. Lu), wqyang@swjtu.edu.cn (W. Yang).

https://doi.org/10.1016/j.jcis.2022.06.170

intrinsic ionic flexibility of $CsPbX_3$ NCs makes them susceptible to the chemical environments [12,13]. For example, polar media, such as water and alcohols, destroy the $CsPbX_3$ NC structure and lead to lattice distortions [14,15]. Moreover, the surface capping ligands of $CsPbX_3$ NCs have a high dynamic binding capacity[16]. Conventional ligands have long-chain molecules of oleate (OA) and oleylammonium (OAm), which are in an acid-base equilibrium: OA + OAm $\rightleftharpoons$ carboxylate anions (OA^-) + oleylammonium ions ($OAmH^+$); $OAmH^+$ + bromide anions (Br^-) $\rightleftharpoons$ OAm + hydrogen bromide (HBr) [17]. Generally, $OAmH^+$ ions combine with Br^- ions, whereas OA^- ions combine with lead ions (Pb^{2+}). These dynamic characters impel reversible protonated and deprotonated processes [18], affording the ligands desorption from the NC surfaces as well as the formation of vacancy defects. Therefore, in the synthesis of high-quality $CsPbBr_3$ NCs, a passivator has to be used to reduce the vacancy defects.

HBr has been used as a source of bromine in the three-precursor method used to prepare stable and efficient $CsPbBr_3$ NCs [19], in the etching of imperfect octahedron structure used to remove surface defects [18] and the in situ passivation of $[PbBr_6]^{4-}$ octahedrons used to obtain blue nanoplatelets with 96% PLQY [20]. However, the role of HBr in the $CsPbBr_3$ NC growth is still unclear. Furthermore, the effect of polar water molecules (H_2O) and hydrogen ions (H^+) present in HBr on $CsPbBr_3$ system is still unclear. A deep understanding of these two mechanisms would enable us to control the synthetic conditions required for preparing high-performance $CsPbBr_3$ NCs. Accordingly, a system for the real-time monitoring of the $CsPbBr_3$ NC growth process is urgently required. In situ photoluminescence (PL) spectra can provide time-resolved information on perovskite NCs growth [21–26]. It is a characterisation method used to study the growth dynamics of perovskite NCs. Recently, $CsPbBr_3$ NC superstructures have been uncovered through in situ tracking during their growth [21]. Moreover, PL spectra can be used to revisit the perovskite NC formation process, which will be in two stages: nucleation and growth stage [24]. Therefore, in situ PL spectra would provide a significant insight into the role of HBr in the growth of $CsPbBr_3$ NCs.

We study the role of HBr in the growth of $CsPbBr_3$ NCs by employing an in situ cryogenic PL spectra.HBr promotes the nucleation rate of $CsPbBr_3$ NCs by approximately two times and enables the emission peak of $CsPbBr_3$ NCs to make a $\sim$ 30 nm redshift. In situ cryogenic PL spectra particularly demonstrate that HBr accelerates the nucleation rates of $CsPbBr_3$ NCs and extends their growth stage, affording the generation of large grains·H_2O (75 or 150 μL) in HBr has almost no effect on $CsPbBr_3$ NC growth and the excess H^+ ions destroy $[PbBr_6]^{4-}$ octahedron structures and cause their fluorescence quenching. $CsPbBr_3$ NCs containing HBr possess a fewer number of trap states than $CsPbBr_3$ NCs that do not contain any HBr. Finally, we fabricate perovskite light-emitting diodes (PeLEDs) using $CsPbBr_3$ NCs with HBr as an emission layer with a peak external quantum efficiency (EQE) of 5.3% and a maximum luminance of 53595 cd m^{-2}. A study on the role of HBr in the growth of $CsPbBr_3$ NCs can provide new insights into the growth dynamics of perovskite NCs.

2. Results and discussion

To observe the role of HBr in the growth of $CsPbBr_3$ NCs, we design an in situ cryogenic photoluminescent system that uses liquid nitrogen (LN) and creates a cryogenic environment (Fig. 1(a)) [11]. LN is used to suppress ultrafast nucleation and growth in $CsPbBr_3$ NCs, which would enable the tracking of PL spectra evolution over a long period. Fig. S1 shows the temperature variety curve plotted for the entire process. Fig. 1(b) and 1(c) show the in situ time evolution of cryogenic PL spectra of $CsPbBr_3$ NCs without (w/o) and with HBr (75 μL) and the redshift of their PL peaks, which finally reach a maximum limit. The redshift indicates an increase in the grain size, and thus a large shift would signify the formation of large grains [27,28]. Generally, a long PL emission indicates a large crystal size. The final PL emission peaks (strongest peak) of $CsPbBr_3$ NCs w/o and with HBr are located at approximately 455 and 485 nm, respectively. The related photographs display blue and cyan PL emissions under ultraviolet (UV) light as shown in the insets of Fig. 1(b) and (c). During the first 20 s, no PL emission peak of $CsPbBr_3$ NCs w/o HBr is present, suggesting that $CsPbBr_3$ NCs have not nucleated during that period (Fig. S2 (a)). The in situ absorption spectrum of the $CsPbBr_3$ NCs w/o HBr in Fig. S3 has not obvious absorption peaks at 20 s, further proving that $CsPbBr_3$ NCs have not nucleated during this period. During the next 20 s, the weakest PL emission with the broadest FWHM appears at approximately 427 nm, indicating that the particle size distribution has become the widest. Thereafter, the PL intensity gradually increases before reaching its maximum value at 240 s (Fig. 1(b)). However, the $CsPbBr_3$ NCs with HBr exhibit a weak emission peak at about 445 nm during the first 20 s and a stable emission peak centered at 485 nm at 120 s (Fig. 1(c) and Fig. S2 (b)). The appearance of the two peaks can be attributed to the acceleration of the nucleation and growth rates of the $CsPbBr_3$ NCs by HBr. Thus, emission wavelength has increased, indicating an increased grain size caused by the addition of HBr.

The main ions and molecule in the HBr solution are H^+ and Br^- ions and H_2O molecules. To investigate in detail how the H_2O in HBr affect the growth of $CsPbBr_3$ NCs, we conduct experiments in which H_2O (55 or 110 μL) replace HBr (75 or 150 μL). The detailed calculations are presented in the supporting information provided. As illustrated in Figs. S4(a) and S4(b), $CsPbBr_3$ NCs containing 55 μL H_2O are not different from those containing 110 μL H_2O. The final emission peaks of both types of NCs are at approximately 456 nm as with $CsPbBr_3$ NC w/o HBr. The other emission peak present at approximately 506 nm is too weak to be considered. Thus, we can reasonably conclude that H_2O in place of 75 μL or 150 μL HBr do not affect the growth of $CsPbBr_3$ NCs.

We also conduct in situ cryogenic PL experiments on $CsPbBr_3$ NCs by adding 150, 300 and 500 μL HBr to study how an excessive amount of H^+ ions could destroy the crystal structure of $CsPbBr_3$ NCs. With the addition of 150, 300 and 500 μL of HBr, the final emission peaks shift to 483, 463 and 450 nm, respectively (Fig. S5 (a)-(c)). Fig. S5(d) shows the photographs of $CsPbBr_3$ NCs (10 min later) with 150, 300, and 500 μL of HBr under daylight and UV light, indicating substantially weakened or even disappeared peaks of PL intensity. We further execute in situ PL spectra experiments with adding excess zinc bromide ($ZnBr_2$) and manganese bromide ($MnBr_2$). As shown in Fig. S5, the final PL peaks of $CsPbBr_3$ NCs with $ZnBr_2$ and $MnBr_2$ can reach 520 nm and 501 nm, respectively. Moreover, Zeng et al. reported excess H^+ in HBr dissolved and destroyed the lattice structure of $CsPbBr_3$ NC [20]. Thus, we believe that it is the excess H^+ ions not the Br^- ions that destroy the crystal structure in our work. The positions of the final PL peaks of $CsPbBr_3$ NCs with 75 and 150 μL HBr are approximately same owning to the small difference between 75 μL and 150 μL; the PL intensity of $CsPbBr_3$ NCs with 150 μL HBr is below that of $CsPbBr_3$ NCs with 75 μL HBr (Fig. S7). Thus, the addition of only the required amount of HBr would help improve the nucleation and growth rates of $CsPbBr_3$ NCs.

Fig. 2(a) and 2(b) show the contour maps of the in situ cryogenic PL spectra of $CsPbBr_3$ NCs w/o and with HBr. The variation of PL emission wavelength with time is illustrated in Fig. 2(c). In the case of $CsPbBr_3$ NCs w/o HBr, Δt (time taken to detect the first PL emission) is longer than that of $CsPbBr_3$ NCs with HBr, revealing that the nucleation and growth rate of $CsPbBr_3$ NCs improved after HBr is added. The positions of the PL peaks of both types of $CsPbBr_3$

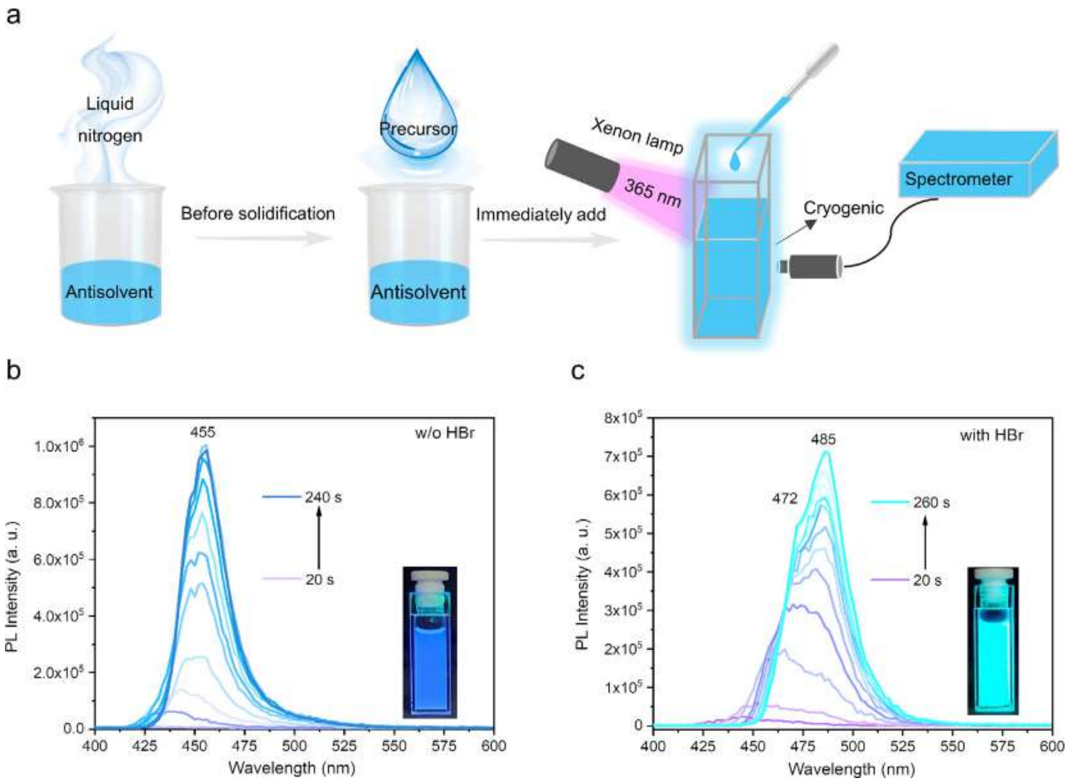

Fig. 1. Detection of cesium lead bromide perovskite ($CsPbBr_3$) NCs with and without HBr using in situ cryogenic photoluminescence (PL) spectra. (a) Schematic illustrating the design of the in situ cryogenic photoluminescent system. In situ observation of time evolution of PL emission of $CsPbBr_3$ NCs (b) without (w/o) HBr and (c) with HBr. (Both the experiments of $CsPbBr_3$ NCs w/o HBr and with HBr were repeated 6 times, and the results were the same as (b) and (c), respectively. The insets in (b) and (c) show the images of final PL emissions of $CsPbBr_3$ NCs without and with HBr under ultraviolet light.).

NCs take approximately 120 s to stabilise. The peaks that gradually redshift indicate a widening of the particle size distributions (defocusing), confirming the findings of previous studies [24,29]. The cyan arrow pointing to the ΔE in Fig. 2(c) refers to the energy difference values between the initial and final PL emissions. ΔE can be calculated using the following equation.

$\Delta E = \frac{hc}{\lambda_1} - \frac{hc}{\lambda_2}$, where h, c, λ_1 and λ_2 are the Planck constant, speed of light, initial PL wavelength of the PL emission and final PL wavelength of the PL emission, respectively. The ΔE of $CsPbBr_3$ NCs w/o and with HBr obtained using the equation are 152.4 meV and 229.3 meV, respectively. The value of ΔE obtained for $CsPbBr_3$ NCs with HBr is much higher than the previous reported values (140–150 meV) [23], indicating a remarkable change from initial grain size to final grain size caused by HBr.

Subsequently, we proceed to observe how PL intensity changed with time (Fig. 2(d)). The PL intensity can change due to three factors: nucleation/increasing nucleation density, crystal growth and slow crystal growth accompanied by photodarkening and thermally induced effects [23]. In our study, the PL intensity increases through three stages. The initial rapid increase in the PL intensity could be attributed to the fast nucleation of perovskite lattices and increased nucleation density triggered by the supersaturation of monomer concentrations (stage Ⅰ). Thereafter, the PL intensity rises again owing to crystal growth (stage Ⅱ). Finally, PL intensity starts to increase slowly, belonged to the slow crystal growth due to the photodarkening and thermally induced effects (stage III). Fig. 2 (e) and 2 (f) demonstrate the time evolution of PL intensity of the $CsPbBr_3$ NCs w/o and with HBr. The stage Ⅰ of the $CsPbBr_3$ NCs w/o HBr is longer than that of $CsPbBr_3$ NCs with HBr, indicating a slower nucleation rate in $CsPbBr_3$ NCs w/o HBr than that in $CsPbBr_3$ NCs with HBr. On the contrary, as shown in Fig. 2 (f), $CsPbBr_3$ NCs with HBr show a longer growth stage (stage Ⅱ) than $CsPbBr_3$ NCs w/o HBr, leading to the formation of large grains. Thus, HBr accelerates nucleation rate and extends growth stage of $CsPbBr_3$ NCs, affording the generation of large grains.

We also prepare the $CsPbBr_3$ NCs taken under LN, LN-HBr, ice water (IW), IW-HBr, room temperature (RT) and RT-HBr conditions to investigate their structures, morphologies and optical performances. The X-ray powder diffraction (XRD) patterns and Raman spectra are monitored, as indicated in Fig. S8. The XRD patterns of $CsPbBr_3$ NCs match well with the cubic $CsPbBr_3$ phase (powder diffraction files No. 75–0412) (Fig. S6(a)). Raman spectra of $CsPbBr_3$ NCs excited with 633 nm laser light are shown in Fig. S6(b). The strong peaks at approximately 72 cm^{-1} (υ_1) can be attributed to the vibrational mode of $[PbBr_6]^{4-}$ octahedrons [30,31]. The vibrational mode υ_2 at about 127 cm^{-1} could be attributed to the motion of Cs^+ cations [31]. The Raman spectra confirm the formation of $CsPbBr_3$ NCs again. Fig. 3(a), (d) and (g) show the PL spectra of all the $CsPbBr_3$ NCs. Unlike in the case of $CsPbBr_3$ NCs w/o HBr, the emission wavelengths of $CsPbBr_3$ NCs with HBr have remarkable redshifts under three different conditions (LN, IW and RT), suggesting increased grain sizes. The corresponding transmission electron microscopy (TEM) images and statistics of the size distribution histogram statistics are shown in Fig. 3(b)–(c), (e)–(f) and (h)–(i) and Fig. S9. The mean grain sizes of $CsPbBr_3$ NCs obtained under LN, LN-HBr, IW, IW-HBr, RT and RT-HBr conditions are 2.18, 3.62, 4.18, 5.51, 6.04 and 10.03 nm, respectively. HBr and reaction temperature determine the size of $CsPbBr_3$ NCs. At any given temperature, the particle size of $CsPbBr_3$ NC increase when the HBr is present, indicating HBr-driven nucleation growth but contradicting previously reported results [32,33]. Our results on the morphologies and sizes are also different from the previously reported results, originated from different synthesis methods and the reaction temperatures[20,34].

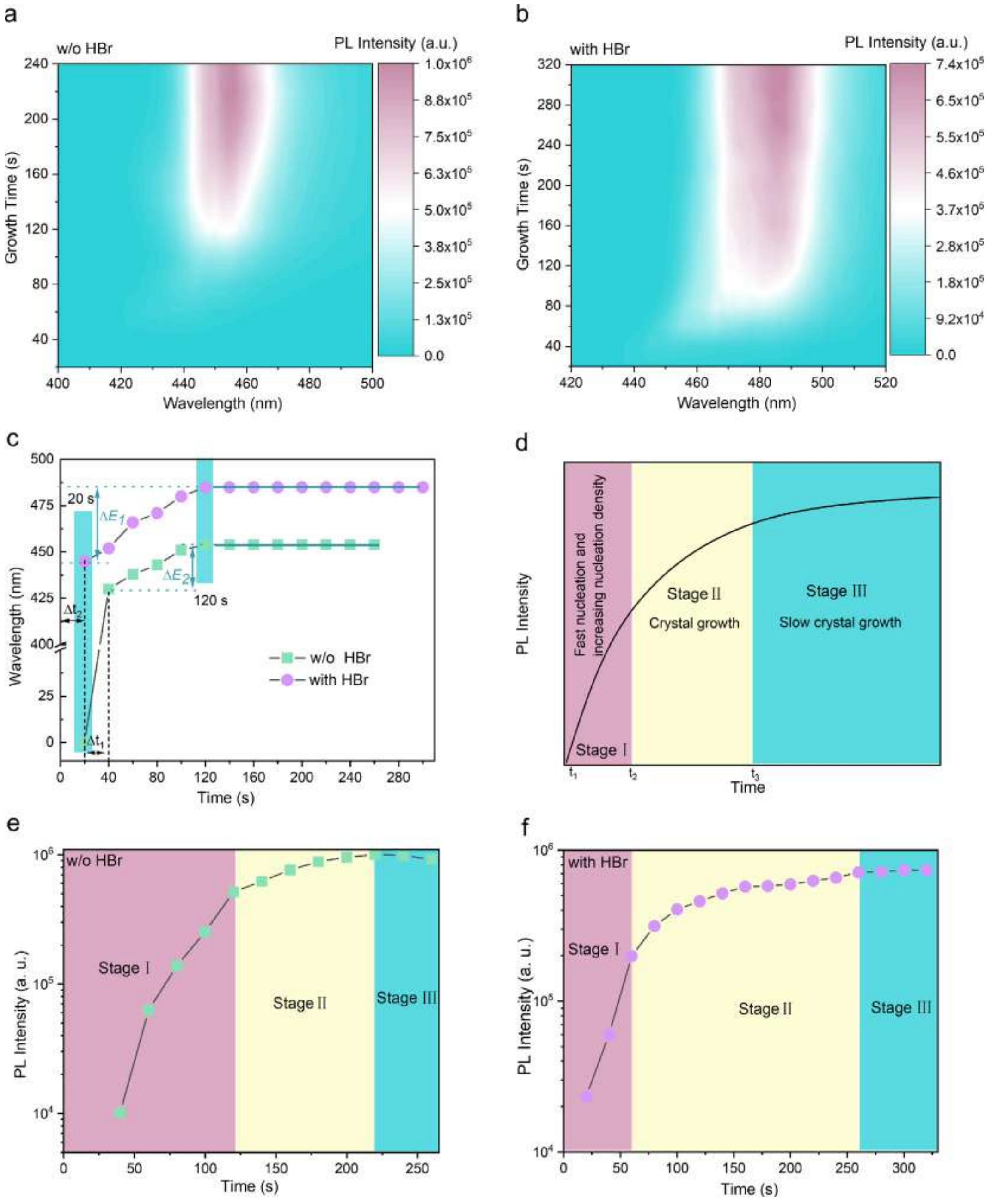

Fig. 2. Role of HBr on the growth of $CsPbBr_3$ NCs. Contour maps of in situ cryogenic PL spectra of $CsPbBr_3$ NCs (a) w/o HBr and (b) with HBr with time. (c) PL emission wavelength versus time. (d) Schematic showing the PL intensity as a function of time during the nucleation and growth stages. (e-f) Time evolution of PL intensity of the $CsPbBr_3$ NCs (e) w/o HBr and (f) with HBr.

The correlation between the reaction temperature and the Br^- concentration ($[Br^-]$) is presented in Fig. 4(a) and 4(b). As can be seen in Fig. 4, $CsPbBr_3$ NC sizes positively correlate with the Br^- concentration ($[Br^-]$) and temperature (T). Here, $[Br^-]$ involves the ionization of HBr and the original bromine ions of the solution. Based on the above mentioned analysis, a simple thermodynamic equilibrium model is considered suitable for illustrating the dependence of $CsPbBr_3$ NCs size on $[Br^-]$ and T [35]. In this model, $CsPbBr_3$ NCs size are determined by the equal chemical potentials of $[Br^-]$ between $CsPbBr_3$ NCs lattices and solution medium. The corresponding equations would be as follows:

$$\mu_{Br^-,sol}([Br^-],T) = \mu_{Br^-,NC}(l,T) \tag{1}$$

$$\mu_{Br^-,sol}([Br^-],T) = \mu^*_{Br^-,sol}(\mathrm{T}) + \mathrm{RTln}(\gamma[Br^-]) \tag{2}$$

where $\mu_{Br^-,sol}([Br^-],T)$ is the Br^- chemical potential of $CsPbBr_3$ NCs with or w/o HBr in the solution at a fixed temperature. $\mu_{Br^-,NC}(l,T)$ is the Br^- chemical potential of $CsPbBr_3$ NC lattice with size (l) at a given temperature. Equation (2) indicates that $\mu_{Br^-,sol}([Br^-],T)$ increases logarithmically with $[Br^-]$ at a given temperature. $\mu^*_{Br^-,sol}(T)$, R and γ in equation (2) are the standard chemical potential of Br^- at temperature T, gas constant and activity coefficient, respectively.

In $CsPbBr_3$ NCs with HBr, the chemical potential of Br^- is higher than that of $CsPbBr_3$ NCs with no HBr, indicating a higher degree of spontaneous progress and increased particle size of $CsPbBr_3$ NCs.

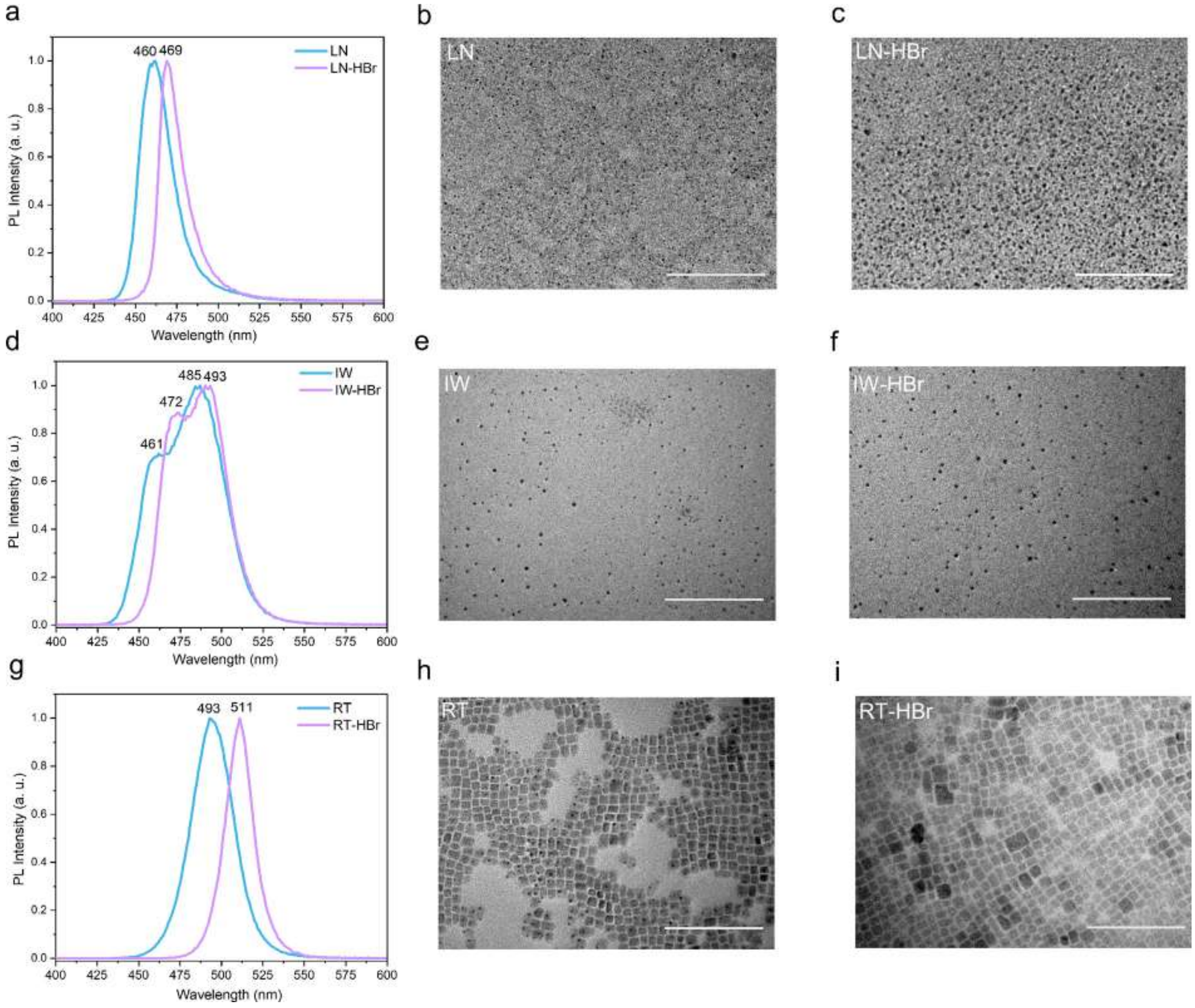

Fig. 3. Morphological and optical characterisation of $CsPbBr_3$ NCs. (a), (d) and (g) Normalised PL spectra and (b), (c), (e), (f), (h) and (i) transmission electron microscopy (TEM) images of $CsPbBr_3$ NCs with or w/o HBr taken under LN, ice water (IW) and room temperature (RT) conditions, respectively. All scale bars are equal to 100 nm. (All the experiments of $CsPbBr_3$ NCs w/o HBr and with HBr taken under LN, IW and RT conditions were repeated 6 times, and the results were the same as shown, respectively.).

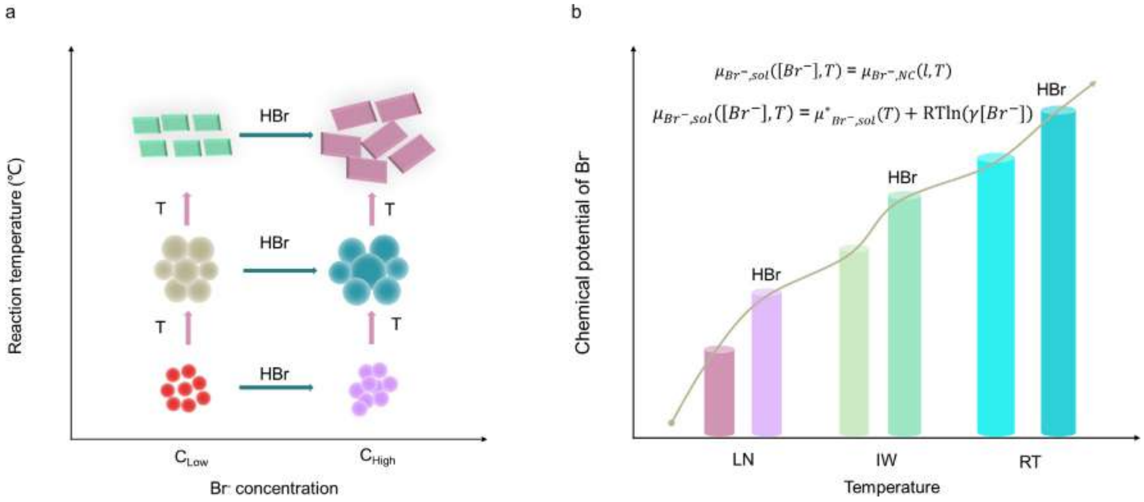

Fig. 4. Increase in the size of $CsPbBr_3$ NCs determined using a thermodynamic equilibrium model. (a) Dependence of the $CsPbBr_3$ NC size on the Br^- concentration (ionisation of HBr and the original bromine ion in the solution) and the reaction temperature. (b) Schematic showing the $CsPbBr_3$ NC size determined based on the equal chemical potentials of Br^- between the $CsPbBr_3$ NC lattice and solution medium.

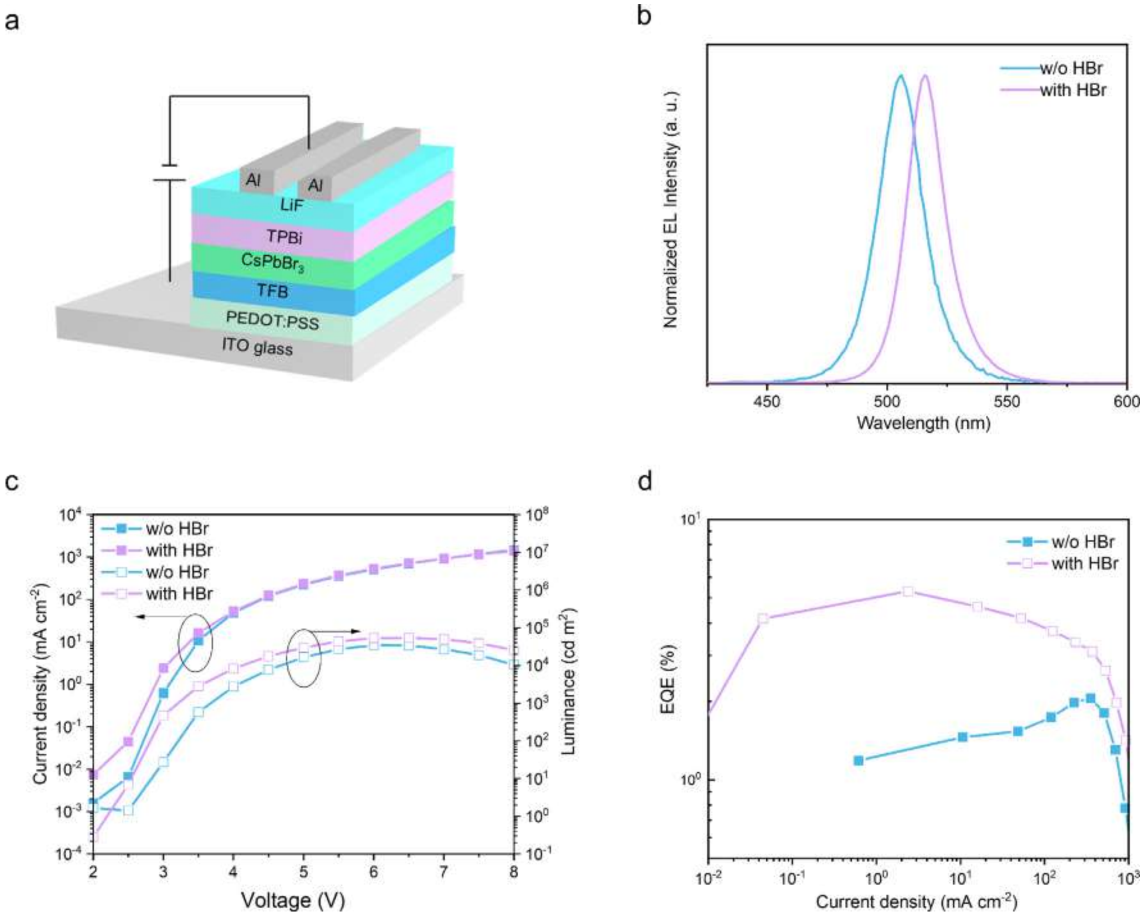

Fig. 5. Performance of PeLEDs fabricated with CsPbBr$_3$ NCs with and w/o HBr. (a) PeLED device structure. (b) EL spectra. (c) Current density/luminance versus voltage curves. (d) EQE versus current density curves.

This thermodynamic equilibrium model is in good agreement with our experimental results. Additionally, time-resolved PL (TRPL) decays are performed to reveal the trap states in CsPbBr$_3$ NCs (Fig. S10). The PL lifetimes of all CsPbBr$_3$ NCs, except those of CsPbBr$_3$ NC treated with LN-HBr, are fitted by biexponential decay functions. The PL lifetime of CsPbBr$_3$ NCs treated with LN-HBr is fitted using a single exponential function. The detailed fitting results are presented in Table S1. Thus, the average PL lifetime of CsPbBr$_3$ NCs with HBr is much higher than that of CsPbBr$_3$ NCs w/o HBr at a fixed temperature, showing substantially reduced trap states caused by HBr based on the presence of ligands: oleylamine (OAm) and oleic acid (OA) and HBr. When HBr with strong acidity is added to the solution, the acid-base equilibrium mentioned above is immediately disrupted and a rapid protonation of OAm (OAm + HBr → OAmH$^+$+ Br$^-$) occurs. Partial OAmH$^+$ ions react with OA$^-$ ions: OA$^-$ + OAmH$^+$ → OAm + OA. This leads to the desorption of few OA$^-$anions. Thus, imperfect [PbBr$_6$]$^{4-}$ octahedrons with bromine vacancy are reduced and removed [18]. Moreover, HBr creates a bromine-rich condition to further eliminate bromine vacancies in CsPbBr$_3$ NCs. These results indicate the addition of HBr increases the grain sizes of CsPbBr$_3$ NCs while substantially decreasing their trap states.

Finally, we fabricate perovskite light-emitting diodes (PeLEDs) with a device structure of indium tin oxide (ITO) glass substrate/ poly(3,4-ethylenedioxythiophene) poly(styrenesulfonate) (PEDOT: PSS)/ Poly[(9,9-dioctylfluorenyl-2,7-diyl)-*alt*-(4,4′-(N-(4-butylphenyl) (TFB)/CsPbBr$_3$ NCs/lithium fluoride (LiF)/aluminium (Al), as illustrated in Fig. 5(a). Fig. 5(b) depicts the normalised electroluminescence (EL) spectra (at 6 V), which exhibits green emission peaking at 505 nm in CsPbBr$_3$ NCs w/o HBr and at 518 nm in CsPbBr$_3$ NCs with HBr. The EL spectra of CsPbBr$_3$ NCs w/o and with HBr at different operating voltages are also shown in Fig. S11. According to the figure, the EL intensity has a tendency to initially increase and subsequently decrease and the emission wavelengths stay constant under operating voltages in the range of 3–7 V. The current density–voltage–luminance curves show that the device fabricated with CsPbBr$_3$ NCs containing HBr possesses a lower turn-on voltage than the device with CsPbBr$_3$ NCs containing no HBr (Fig. 5(c)). This difference in the turn-on voltage could be attributed to the decreased number of trap states and suppressed leakage current in CsPbBr$_3$ NCs with HBr. The maximum luminance of PeLEDs with HBr was 53595 cd m^{-2}, which is higher than that of PeLEDs w/o HBr (34306 cd m^{-2}). Furthermore, the PeLEDs with HBr show a peak EQE of 5.3%, while the peak EQE of the PeLED w/o HBr is only 2.1% (Fig. 5(d)). This dramatic improvement in the performance of PeLEDs with HBr can be attributed to the outstanding emission properties and improved carrier balance of HBr [36].

3. Conclusion

In summary, we study the role of HBr in the growth of CsPbBr$_3$ NCs by performing an in situ cryogenic PL spectra using LN. In contrast to w/o HBr, HBr improved the nucleation rate of CsPbBr$_3$ NCs by approximately two times and its PL emission peak exhibited a ~ 30 nm redshift. At the same time, we can conclud that HBr accelerates the nucleation rate and extends the growth stage of

$CsPbBr_3$ NCs, affording the generation of large grains. Moreover, the TRPL results prove that the addition of HBr to $CsPbBr_3$ NCs substantially reduces the number of trap states. Improved PeLED performances also demonstrate the role of HBr in producing high-quality $CsPbBr_3$ NCs. These findings confirm that HBr plays a significant role of growth dynamics of $CsPbBr_3$ NCs. The in situ cryogenic PL spectra performed using LN helps build a bridge between microscopic growth dynamics and the final steady-state of NCs, which can guide the design of high-quality NCs for use in efficient optoelectronic devices.

CRediT authorship contribution statement

Jingjing Cao: Conceptualization, Methodology, Software, Writing – original draft, Data curation, Writing – review & editing. **Qungui Wang:** Data curation, Software, Visualization. **Wen Li:** Visualization, Investigation, Resources. **Cheng Yan:** Software, Validation, Resources. **Xiankan Zeng:** Software, Validation, Resources. **Yue Gao:** Validation, Resources. **Xiaotong Zheng:** Validation, Resources. **Jun Lu:** Supervision, Writing – review & editing, Funding acquisition. **Weiqing Yang:** Supervision, Writing – review & editing, Funding acquisition, Project administration.

Declaration of Competing Interest

The authors declare that they have no known competing financial interests or personal relationships that could have appeared to influence the work reported in this paper.

Acknowledgements

This work was financially supported by the National Natural Science Foundation of China (No. 52073237), Young Scientific and Technological Innovation Research Team Funds of Sichuan Province (No. 20CXTD0106 and 2019YFG0292), and Fundamental Research Funds for the Central Universities (2682020CX06). The first author is very grateful to her husband, Mr. Chen. We are thankful to Analytical and Testing Center of Southwest Jiaotong University for supporting the XRD and TEM measurements.

Appendix A. Supplementary data

Supplementary data to this article can be found online at https://doi.org/10.1016/j.jcis.2022.06.170.

References

[1] M.V. Kovalenko, L. Protesescu, M.I. Bodnarchuk, Properties and potential optoelectronic applications of lead halide perovskite nanocrystals, Science 358 (6364) (2017) 745–750.

[2] Y. Li, X. Zhang, H. Huang, S.V. Kershaw, A.L. Rogach, Advances in metal halide perovskite nanocrystals: Synthetic strategies, growth mechanisms, and optoelectronic applications, Mater. Today 32 (2020) 204–221.

[3] M. Jiang, Z. Hu, L.K. Ono, Y. Qi, CsPbBrxI3-x thin films with multiple ammonium ligands for low turn-on pure-red perovskite light-emitting diodes, Nano Res. 14 (1) (2021) 191–197.

[4] J. Chen, J. Wang, X. Xu, J. Li, J. Song, S. Lan, S. Liu, B. Cai, B. Han, J.T. Precht, D. Ginger, H. Zeng, Efficient and bright white light-emitting diodes based on single-layer heterophase halide perovskites, Nat. Photonics 15 (3) (2021) 238–244.

[5] X.K. Zeng, W. Li, C. Yan, J.J. Cao, X.H. Fu, W.Q. Yang, Crystallization control via a molecular needle knitting strategy for the enhanced emission efficiency and stability of CsPbBr 3 films, J. Mater. Chem. C 9 (44) (2021) 15967–15976.

[6] C. Yan, C. Luo, W. Li, X. Peng, J. Cao, X. Zeng, Y. Gao, X. Fu, X. Chu, W. Deng, F. Chun, S. Yang, Q. Wang, W. Yang, Thermodynamics-induced injection inhanced deep-blue perovskite quantum dot LEDs, Acs. Appl. Mater, Inter, 2021.

[7] M.B. Faheem, B. Khan, C. Feng, M.U. Farooq, F. Raziq, Y. Xiao, Y. Li, All-inorganic perovskite solar cells: energetics, key challenges, and strategies toward commercialization, ACS Energy Lett. 5 (1) (2020) 290–320.

[8] L. Yan, Q. Xue, M. Liu, Z. Zhu, J. Tian, Z. Li, Z. Chen, Z. Chen, H. Yan, H.-L. Yip, Y. Cao, Interface engineering for all-inorganic $CsPbI_2Br$ perovskite solar cells with efficiency over 14%, Adv. Mater. 30 (33) (2018) 1802509.

[9] M.I. Saidaminov, M.A. Haque, M. Savoie, A.L. Abdelhady, N. Cho, I. Dursun, U. Buttner, E. Alarousu, T. Wu, O.M. Bakr, Perovskite photodetectors operating in both narrowband and broadband regimes, Adv. Mater. 28 (37) (2016) 8144–8149.

[10] Q.A. Akkerman, G. Rainò, M.V. Kovalenko, L. Manna, Genesis, challenges and opportunities for colloidal lead halide perovskite nanocrystals, Nat. Mater. 17 (5) (2018) 394–405.

[11] J. Cao, C. Yan, C. Luo, W. Li, X. Zeng, Z. Xu, X. Fu, Q. Wang, X. Chu, H. Huang, X. Zhao, J. Lu, W. Yang, Cryogenic-temperature thermodynamically suppressed and strongly confined $CsPbBr_3$ quantum dots for deeply blue light-emitting diodes, Adv. Opt. Mater. 2100300.

[12] M. Kazes, T. Udayabhaskararao, S. Dey, D. Oron, Effect of surface ligands in perovskite nanocrystals: extending in and reaching out, Accounts Chem. Res. 54 (6) (2021) 1409–1418.

[13] K. Miyata, T.L. Atallah, X.-Y. Zhu, Lead halide perovskites: crystal-liquid duality, phonon glass electron crystals, and large polaron formation, Sci. Adv. 3 (10) (2017) e1701469.

[14] A. Loiudice, S. Saris, E. Oveisi, D.T.L. Alexander, R. Buonsanti, CsPbBr 3 QD/Al_Ox inorganic nanocomposites with exceptional stability in water, light, and heat, Angew. Chem. Int. Ed. 56 (36) (2017) 10696–10701.

[15] S. Wang, L. Du, Z. Jin, Y. Xin, H. Mattoussi, Enhanced stabilization and easy phase transfer of CsPbBr 3 perovskite quantum dots promoted by high-affinity polyzwitterionic ligands, J. Am. Chem. Soc. 142 (29) (2020) 12669–12680.

[16] J. De Roo, M. Ibáñez, P. Geiregat, G. Nedelcu, W. Walravens, J. Maes, J.C. Martins, I. Van Driessche, M.V. Kovalenko, Z. Hens, Highly dynamic ligand binding and light absorption coefficient of cesium lead bromide perovskite nanocrystals, Acs Nano 10 (2) (2016) 2071–2081.

[17] F. Krieg, S.T. Ochsenbein, S. Yakunin, S. ten Brinck, P. Aellen, A. Süess, B. Clerc, D. Guggisberg, O. Nazarenko, Y. Shynkarenko, S. Kumar, C.-J. Shih, I. Infante, M. V. Kovalenko, Colloidal $CsPbX_3$ (X = Cl, Br, I) nanocrystals 2.0: zwitterionic capping ligands for improved durability and stability, ACS Energy Lett. 3 (3) (2018) 641–646.

[18] C. Bi, Z. Yao, X. Sun, X. Wei, J. Wang, J. Tian, Perovskite quantum dots with ultralow trap density by acid etching-driven ligand exchange for high luminance and stable pure-blue light-emitting diodes, Adv. Mater. 33 (15) (2021) 2006722.

[19] C. Luo, C. Yan, W. Li, F.J. Chun, M.L. Xie, Z.H. Zhu, Y. Gao, B.L. Guo, W.Q. Yang, Ultrafast thermodynamic control for stable and efficient mixed halide perovskite nanocrystals, Adv. Funct. Mater. 30 (19) (2020) 2000026.

[20] Y. Wu, C. Wei, X. Li, Y. Li, S. Qiu, W. Shen, B. Cai, Z. Sun, D. Yang, Z. Deng, H. Zeng, In situ passivation of PbBr ^{64}– octahedra toward blue luminescent $CsPbB_r3$ nanoplatelets with near 100% absolute quantum yield, ACS Energy Lett. 3 (9) (2018) 2030–2037.

[21] H. Huang, M.W. Feil, S. Fuchs, T. Debnath, A.F. Richter, Y. Tong, L. Wu, Y. Wang, M. Döblinger, B. Nickel, Growth of perovskite CsPbBr 3 nanocrystals and their formed superstructures revealed by in situ spectra, Chem. Mater. 32 (20) (2020) 8877–8884.

[22] K. Suchan, J. Just, P. Becker, E.L. Unger, T. Unold, Optical in situ monitoring during the synthesis of halide perovskite solar cells reveals formation kinetics and evolution of optoelectronic properties, J. Mater. Chem. A 8 (20) (2020) 10439–10449.

[23] T.-B. Song, Z. Yuan, M. Mori, F. Motiwala, G. Segev, E. Masquelier, C.V. Stan, J.L. Slack, N. Tamura, C.M. Sutter-Fella, Revealing the dynamics of hybrid metal halide perovskite formation via multimodal in situ probes, Adv. Funct. Mater. 30 (6) (2020) 1908337.

[24] X. Wang, Y. Liu, N. Liu, R. Sun, W. Zheng, H. Liu, Y. Zhang, Revisiting the nanocrystal formation process of zero-dimensional perovskite, J. Mater. Chem. A 9 (8) (2021) 4658–4663.

[25] Q. Hu, L. Zhao, J. Wu, K. Gao, D. Luo, Y. Jiang, Z. Zhang, C. Zhu, E. Schaible, A. Hexemer, C. Wang, Y. Liu, W. Zhang, M. Grätzel, F. Liu, T.P. Russell, R. Zhu, Q. Gong, In situ dynamic observations of perovskite crystallisation and microstructure evolution intermediated from $[PbI_6]^{4-}$ cage nanoparticles, Nat. Commun. 8 (1) (2017) 15688.

[26] K. Meng, L. Wu, Z. Liu, X. Wang, Q. Xu, Y. Hu, S. He, X. Li, T. Li, G. Chen, In situ real-time study of the dynamic formation and conversion processes of metal halidep erovskite films, Adv. Mater. 30 (11) (2018) 1706401.

[27] L. Wagner, L.E. Mundt, G. Mathiazhagan, M. Mundus, M.C. Schubert, S. Mastroianni, U. Würfel, A. Hinsch, S.W. Glunz, Distinguishing crystallization stages and their influence on quantum efficiency during perovskite solar cell formation in real-time, Sci. Rep. 7 (1) (2017) 14899.

[28] T.-Y. Hsieh, C.-K. Huang, T.-S. Su, C.-Y. Hong, T.-C. Wei, Crystal growth and dissolution of methylammonium lead iodide perovskite in sequential deposition: correlation between morphology evolution and photovoltaic performance, Acs Appl. Mater. Interface 9 (10) (2017) 8623–8633.

[29] M. Koolyk, D. Amgar, S. Aharon, L. Etgar, Kinetics of cesium lead halide perovskite nanoparticle growth; focusing and de-focusing of size distribution, Nanoscale 8 (12) (2016) 6403–6409.

[30] D.M. Calistru, L. Mihut, S. Lefrant, I. Baltog, Identification of the symmetry of phonon modes in CsPbCl3 in phase IV by Raman and resonance-Raman scattering, J. Appl. Phys. 82 (11) (1997) 5391–5395.

[31] J.-H. Cha, J.H. Han, W. Yin, C. Park, Y. Park, T.K. Ahn, J.H. Cho, D.-Y. Jung, Photoresponse of CsPbBr 3 and C_s4PbB_r6 perovskite single crystals, J. Phys. Chem. Lett. 8 (3) (2017) 565–570.

[32] A. Dutta, S.K. Dutta, S. Das Adhikari, N. Pradhan, Tuning the size of CsPbBr 3 nanocrystals: all at one constant temperature, ACS Energy Lett. 3 (2) (2018) 329–334.

[33] D. Amgar, A. Stern, D. Rotem, D. Porath, L. Etgar, Tunable length and optical properties of $CsPbX_3$ (X = Cl, Br, I) nanowires with a few unit cells, Nano Lett. 17 (2) (2017) 1007–1013.

[34] X. Xiao, Y. Li, R.-J. Xie, Blue-emitting and self-assembled thinner perovskite CsPbBr 3 nanoplates: synthesis and formation mechanism, Nanoscale 12 (16) (2020) 9231–9239.

[35] Y.T. Dong, T. Qiao, D. Kim, D. Parobek, D. Rossi, D.H. Son, Precise control of quantum confinement in cesium lead halide perovskite quantum dots via thermodynamic equilibrium, Nano Lett. 18 (6) (2018) 3716–3722.

[36] H.M. Li, H. Lin, D. Ouyang, C.L. Yao, C. Li, J.Y. Sun, Y.L. Song, Y.F. Wang, Y.F. Yan, Y. Wang, Q.F. Dong, W.C.H. Choy, Efficient and stable red perovskite light-emitting diodes with operational stability >300 h, Adv. Mater. 33 (15) (2021).